PCCP

Mechanisms of Alumina Growth via Atomic Layer Deposition on Nickel Oxide and Metallic Nickel Surfaces

SCHOLARONE™
Manuscripts

Mechanisms of Alumina Growth via Atomic Layer Deposition on Nickel Oxide and Metallic Nickel Surfaces

Francisco Alejandro Ospina-Acevedo, Saul Perez-Beltran, Perla B. Balbuena*
Department of Chemical Engineering, Texas A&M University, College Station, TX, 77843, USA
*Author for correspondence. E-mail: balbuena@tamu.edu

Abstract

We aim at elucidating the mechanism of the trimethyl aluminum (TMA) decomposition on oxidized nickel (NiO) and metallic nickel (Ni) facets in the absence of a source of hydroxyl groups. This TMA decomposition mechanism constitutes the earliest stage of growth of Al_2O_3 coatings with the atomic layer decomposition (ALD) method, which stabilizes nickel catalysts in energy-intensive processes such as the dry reforming of methane. Our first-principles calculations suggest thermodynamic favorability for the TMA decomposition on metallic nickel compared to oxidized nickel. Moreover, the decomposition of TMA on metallic nickel showed almost no differences in terms of energy barriers between flat and stepped surfaces. Regarding the impact of the CH_3 radicals formed after TMA decomposition, we calculated stronger adsorption on metallic nickel facets than on oxidized nickel, and these adsorption energies are comparable to the adsorption energies calculated in earlier works on Al_2O_3 ALD growth on palladium surfaces. These results lead us to believe in the growth of porous Al_2O_3 coatings triggered by CH_3 contamination rather than due to preferential TMA decomposition on stepped and/or defective facets. The CH_3 radicals are likely to be thermally stable at temperatures used during Al_2O_3 ALD processes, partially passivating the surface towards further TMA decomposition.

Introduction

A potential breakthrough in the development of new technologies that contribute to alleviating climate change is the formulation of a suitable catalyst for the dry reforming reaction (DRM) of CH_4 with CO_2 generating H_2 and CO.[1] Several studies point at nickel nanoparticles as promising DRM catalysts due to the low cost and abundance of nickel compared to other transition metals catalytically active for this reaction such as rhodium or ruthenium.[2-3] However, the high temperatures required for the DRM reaction to proceed, destabilize the nickel nanoparticles and make the whole process unstable due to sintering and carbon deposition.[4-5]

A promising strategy to eliminate sintering and carbon deposition is to partially covering the catalyst surface with a protective coating.[6-8] The underlying idea is to shield the catalyst against the harsh conditions at high temperatures while passivating the highly active but unselective sites on the nanoparticle surface.[4, 9] The key for successfully applying this strategy, however, relies on figuring out a synthesis procedure with strict control of the shell thickness, as an excessively thin shell will not protect the catalyst, while an overly thick one will completely bury the catalytically active surface.[10]

To achieve this thickness control, the atomic layer deposition method (ALD) is one of the few (if not the only one known) with the potential to deliver perfect conformality and accurate film thickness control.[10-12] The ALD method is a modified chemical vapor deposition (CVD) method based on the exposure of the nanoparticle to alternating self-limiting decomposition reactions.[13-14] On nickel nanoparticles, the ALD method usually goes through sequential decomposition of trimethyl aluminum (TMA) and H_2O vapor. It is generally accepted that the TMA molecules react with $-OH^*$ groups to form $Al(CH_3)_x^*$ (x=1-2) structures that later transform into $Al(OH)_x^*$ (x=1-2) after exposure to H_2O. This procedure in turn prepares the surface for another cycle of TMA/H_2O exposure. The extent of the exposure (TMA and H2O doses) determines how much of the surface is covered; the longer exposure time the larger surface area subject to decomposition of TMA, such as that it allows a nearly atomic-level control

over the thickness of the Al_2O_3 coating, critical for ensuring access to the catalytically active facets of the nanoparticle.[14-15]

The effectiveness of the ALD method has been already tested for the DRM reaction.[4] At low temperature regimes (525 °C), nickel catalysts with thick alumina coatings (20 exposure cycles) performed best at inhibiting coke deposition but showed lowered catalytic activity, while at temperatures as high as 800 °C, five deposition cycles showed effectiveness at protecting the nanoparticles against sintering, however failing due to coke deposition. The need to explain this correlation between the Al_2O_3 thickness and its ability to protect the catalysts simultaneously against sintering and deactivation led to investigate the morphology of Al_2O_3 ALD coatings on palladium and platinum nanoparticles.[8, 14, 16] The combined use of experimental techniques and computational modeling methodologies suggested a substrate-inhibited growth mechanism initiating at discrete sites on the nanoparticle surface, forming islands that eventually coalesce into a porous Al_2O_3 film. The computational modeling performed in this study contributed to show that highly reactive edges and corner motifs on the nanoparticle surface act as seeds where the "islands" first form, leaving the less reactive but more selective sites of the nanoparticle available for catalytic activity.

The ALD method is very flexible as it works on various types of metallic or even multi-metallic nanoparticles,[10, 17-18] and while the procedure is thermodynamically favorable on either oxidized or reduced nickel, the most common one is growing the Al_2O_3 coating on the oxidized nanoparticle followed by a reduction step to activate the catalyst.[6] However, little is known about the impact that the initial oxidation state has on the growth mechanism of Al_2O_3 coating, even though its full understanding is fundamental for tuning the catalyst simultaneous resistance against sintering and deactivation.

In this work, we adopted a basic science approach aimed at understanding the fundamentals of the TMA decomposition mechanism on oxidized nickel (NiO) and metallic nickel (Ni) facets in the absence of a source of hydroxyl groups. We started with the elucidation of the adsorption modes of the TMA molecule, the intermediates formed upon sequential scission of the Al-C bonds: dimethyl aluminum (DMA), methyl aluminum (MA), and the CH_3 radical. Then, we proceeded to calculate the reaction energies and activation barriers for all the elementary reactions in the decomposition of the TMA molecule.[14] In general, we found that the surface topology plays a more important role on nickel oxide than on metallic facets regarding the decomposition of the TMA molecule. The CH_3 radicals presented stronger adsorption on metallic than on nickel oxide facets. We believe that this behavior might promote the growth of a porous Al_2O_3 coating due to CH_3 contamination rather than due to preferential growth on stepped and or defective facets over the metallic nickel surface.

Computational Details

All calculations use density functional theory (DFT) method as implemented in the Vienna Ab Initio Simulation Package (VASP – version 5.4.4). We set the cutoff energy to 520 eV for the plane wave basis set describing the valence electrons, whereas the treatment of the core-electron dynamics was done with the projector augmented wave potential method (PAW) .[19] For the exchange-correlation functional, we used the Perdew-Burke-Ernzerhof generalized gradient approximation (PBE-GGA) ,[20-21] while the integration of Brillouin zone integration was done with the Monkhorst-Pack grid method.[22] Earlier calculations with the PBE-GGA on the CH_4 decomposition on Ni surfaces and the analysis of the stability of NiO(111) surfaces showed the reliability of this approximation for modeling Ni and NiO structures.[23-24] The first order Methfessel-Paxton smearing method with an energy smearing set to 0.2 eV allowed for determining the electronic occupancies on calculations on Ni surfaces,[25] whereas on NiO surfaces the tetrahedron method with Block corrections served for the same purpose.[26] The calculations on NiO surfaces required the Hubbard U correction to the PBE-GGA functional due to the strong electron correlation within the partially filled d-shells, typical of transition metal oxides, for which we set the difference between the parameter U and the exchange parameter J to 5.3 eV.[23, 27-31] Both bulk and surface calculations included spin polarization. No zero-point energy corrections were performed.[14]

All geometry optimizations followed through a two-step procedure, with the first and second optimizations performed with their convergence criterions set to 10^{-4} eV, and 0.02 eV/Å, respectively. The adsorption energy was defined as the difference between the coupled slab/adsorbate system minus the bare slab and the adsorbate molecule in gas phase (E_{ads} = E(slab/adsorbate) – [E(slab) + E(molecule in gas phase)]), with a negative value for the adsorption energy corresponding to a thermodynamically favorable adsorption process.[32] The calculation of the gas phase energies for the TMA and all the intermediate molecules was performed in a 20.0 Å x 20.5 Å x 20.10 Å unit cell with the gamma-point for the Brillouin zone and the Gaussian smearing method set to 0.05 eV for the partial occupancies.

The reaction energy was calculated as the energy difference between products and reactants. A negative value for the reaction energy corresponds to an exothermic process, whereas a positive value to an endothermic one. The reaction barrier, on the other side, accounts for the energy difference between the transition state (TS) and reactant. The geometry of the TS was converged with the climbing-image nudged elastic band (CI-NEB) method,[33-34] whereas the Bader charge analysis method allowed for the estimation of the electronic charges.[35-37]

System Details

We modeled the surface of the nanoparticles using idealized flat and stepped facets of nickel oxide and metallic nickel. We did not model the complete nanoparticles in our simulations as earlier theoretical studies pointed out that the TMA decomposition is a purely surface process without subsurface diffusion of either species on any stage of decomposition.[14, 16] As such, modeling the whole nanoparticle would increase the number of atoms in the unit cell without significant improvements in the accuracy of the adsorption energies and reaction barriers.

The NiO unit cell used for modeling the NiO facets converged to a lattice parameter equal to 4.22 Å, in close agreement with the experimentally reported value of 4.17 Å.[27] The NiO(100) facet represented the flat regions over the surface of the NiO nanoparticles, and it consisted of a 4x4 6-layer slab with the three bottom layers fixed and 17 Å vacuum along the z-coordinate. We did not model the presence of OH groups on the NiO(100) facet but rather studied the decomposition of the TMA molecule on lattice oxygen atoms located on the surface. EELS measurements indicate no OH formation on regular NiO(100) surface sites but only on defect sites.[38] For the stepped regions on NiO, we used the 2x2 hydrogen-free NiO(111) facet with an oxygen-terminated octopolar reconstruction surface as earlier studies pointed out to this surface as the most stable at elevated temperatures.[23, 30-31, 39-42] For our modeling purposes, the structural motifs of this surface made it attractive for studying the dynamics of the TMA decomposition.

The nickel nanoparticle was modeled with the flat 4x4 Ni(111) and the stepped 2x2 Ni(211) facets. Similar studies on the TMA decomposition have been using these two facets for representing the surface of platinum and palladium nanoparticles (platinum, palladium, and nickel share the same space group) .[14, 16] We used a three- and a six-layer slab to represent the Ni(111) and Ni(211) surfaces, respectively. For both facets, we fixed the bottom layer and allowed 12 Å vacuum along the z-coordinate.

Results

We addressed first the adsorption of the TMA molecule, the DMA and MA intermediates, and the CH_3 radical on the oxidized and metallic facets with the goal of elucidating the most suited geometries for the calculations of the reaction energies and reaction barriers following the decomposition of the TMA.

TMA, DMA and MA on NiO surface facets

We evaluated the adsorption of the TMA molecule on four adsorption sites over the NiO(100) facet. All optimizations converged to the same geometry with the TMA molecule located on top of a surface oxygen atom with an Al-O distance equal to 1.87 Å. This adsorption mode has adsorption energy (E_{ads}) of -1.24 eV, whereas the adsorption energies for the DMA and MA are -2.21 and -1.45 eV, respectively. The DMA and MA intermediates

converged into an optimized structure with a similar configuration to the TMA molecules, with the Al atom still binding to an oxygen atom but slightly displaced towards the neighboring nickel atoms. Figure 1 shows the optimized geometries for the TMA molecule and the DMA and MA intermediates. For the DMA intermediate, the Al-O and Al-Ni distances are 1.82 and 2.48 Å, respectively. The MA intermediate, on the other side, aligns vertically with the Al-O distance equal to 1.84 Å and the Al atom interacting with two neighboring nickel atoms at an average distance of 2.31 Å (labeled as Ni_1 and Ni_2 in Figure 1). The Bader charge analysis shows a net charge transfer to the oxide surface equal to 0.149 |e|, 0.724 |e|, and 1.543 |e| for the TMA molecule and the DMA and MA intermediates, respectively. It is interesting to observe how this charge transfer into the oxide surface increases with every Al-CH$_3$ bond cleavage. This correlates directly with the TMA effectiveness to act as a reducing agent based on the relatively low dissociation energy of the Al-CH$_3$ bond (approximately 280 kJ/mol).[43] Before adsorption, the average Bader charges associated with nickel and oxygen atoms in NiO(100) are 1.25 |e| and -1.25 |e| respectively. After MA adsorption, however, the neighbor nickel atoms labeled as Ni_1 and Ni_2 (Figure 1) partially reduce to an associated Bader charge equal to 0.554 |e| and 0.553 |e|, respectively.
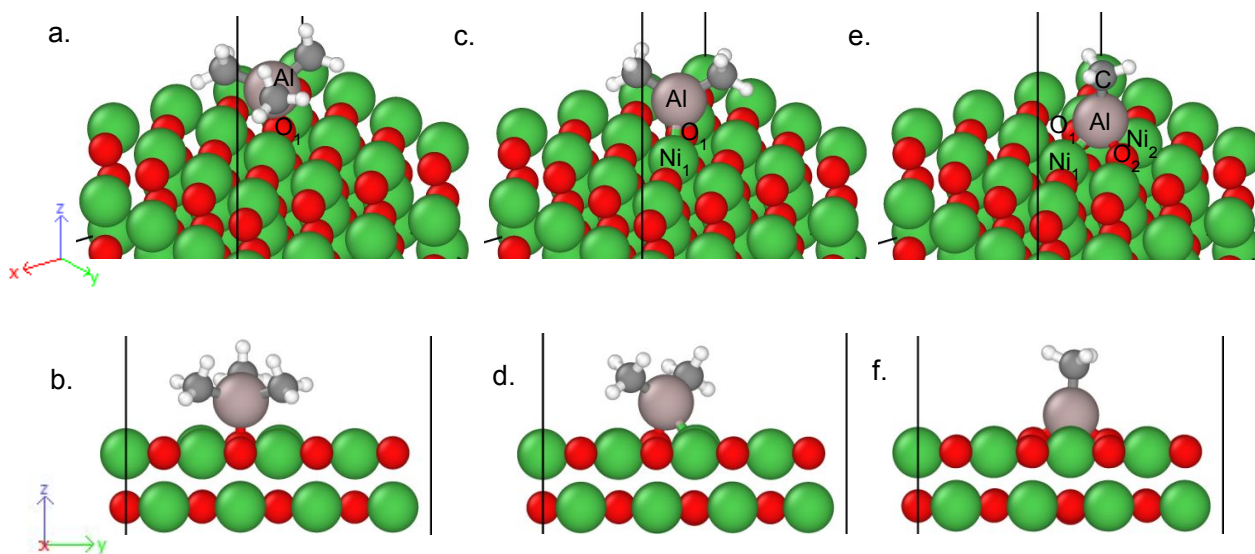
Figure 1: TMA, DMA, and MA adsorption geometries on NiO(100): top and side views for (a,b) TMA, (c,d) DMA, and (e,f) MA

Figure 2 displays the 2x2 NiO(111) with octopolar reconstruction. This reconstruction takes place through the removal of three quarters and one quarter of the atoms present in the first and second layer, respectively, creating a pyramid-like geometry with three nickel atoms as the triangular basis and one oxygen atom on top. This carved-like topology creates different adsorption sites that become increasingly less accessible as they locate in lower atomic layers; the oxygen atoms labeled with the number 1 (black colored numbers) correspond to the ones located at the outermost layer, followed by the oxygen atoms labeled as 2, 3, and 4 in the lower layers. The same ordering applies for the nickel atoms labeled with blue colored numbers.
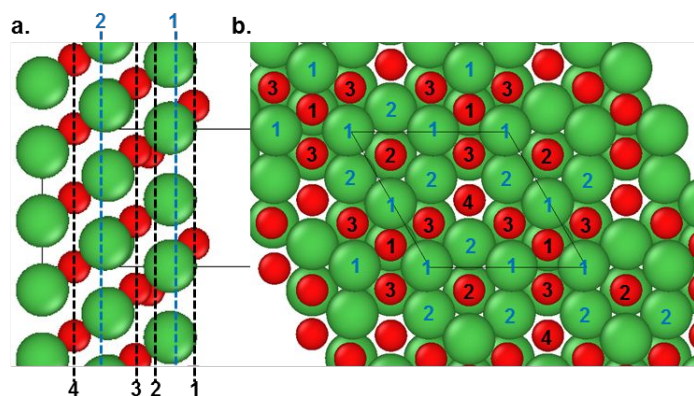
Figure 2: Adsorption sites on the 2x2 NiO(111) surface with octopolar reconstruction: a. side view and b. top view

Figure 3a and b show the top and side views of the TMA molecule adsorbed on an oxygen atom labeled as 1 (see Figure 2 for the labels) on the NiO(111) facet. The adsorption energy for this geometry is -1.30 eV, whereas the adsorption energies for the TMA molecule on the oxygen atoms labeled as 2 and 3 are equal to -0.29 and -0.11 eV, respectively (not shown in Figure 3). This trend in the adsorption energies revealed preferred adsorption on the oxygen atom topping the pyramid-like topology. In the same way, the adsorption mode for the DMA intermediate on the top oxygen atom (site 1) has an adsorption energy equal to -2.82 eV (not shown in Figure 3).

Compared to the TMA molecule, the DMA adsorption on lower atomic layers (oxygen site 2) causes a surface reconstruction that ends with the DMA intermediate interacting with two oxygen atoms at 1.88 and 1.94 Å, respectively (Figure 3c and d). The adsorption energy for this DMA intermediate is -3.61 eV, showing that surface reconstruction leads to a stronger interaction between the molecule and the surface, compared to the calculation on NiO(100). The MA intermediate followed the same behavior of the DMA. The adsorption energy on the top oxygen atom (not shown in Figure 3) was -2.54 eV, and the adsorption on lower atom layers (site 2) triggered a surface reconstruction that ended with the formation of an O-Al-O bridge with an adsorption energy equal to -2.66 eV (Figures 3e and f).
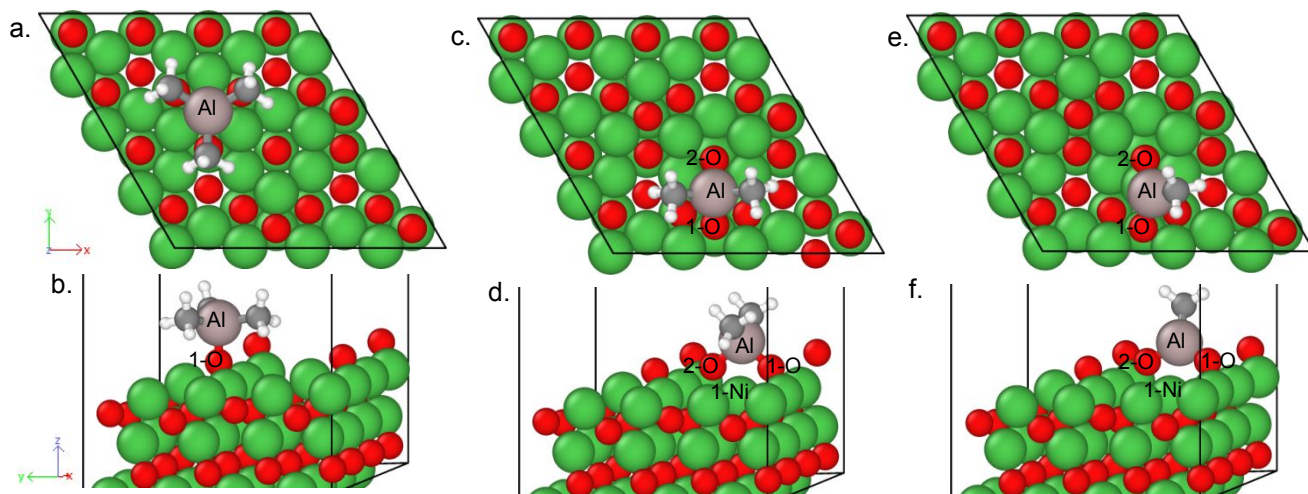
Figure 3: TMA, DMA, and MA adsorption geometries on NiO(111): top (a, c, e) and side (b, d, f) views for (a,b) TMA, (c,d) DMA, and (e,f) MA

As with the NiO(100) surface, the Bader charge transfer to the NiO(111) increases with the cleavage of Al-CH$_3$ bonds. The TMA molecule causes a negligible charge exchange with the NiO(111) surface, but the DMA and MA intermediates transfer up to 0.832 |e| and 1.621 |e| towards the surface. This significant charge transfer correlates with the surface reconstruction observed for these two intermediates; the displacement of the oxygen atoms from the lower atomic layers of the NiO(111) surface leads to a partial reduction of the neighbor nickel atoms, which

could trigger the formation of local "metallic" clusters over the surface. This result evidences the strong reducing character of the TMA molecule suggested by other authors before.[43-45]

TMA, DMA, and MA on Ni surface facets

The adsorption energy of the TMA molecule on either hcp or fcc sites on Ni(111) is -0.95 eV, with two of the Al-C bonds elongating from 1.97 Å to 2.19 and 2.12 Å, respectively (Figure 4a). The adsorption energies for the DMA and MA intermediates are equal to -2.99 and -3.75 eV, respectively, with negligible differences from the hcp or the fcc sites. Compared to the TMA molecule, the DMA and MA intermediates show no significant elongation on either Al-C bond (Figure 4b and c); the longest elongation happens for one of the Al-C bonds of the DMA molecule, and it is equal to 0.04 Å only. In summary, the TMA molecule and the DMA and MA intermediates show stronger adsorption energies as the number of Al-C scissions increases, but this effect does not cause surface reconstruction of the Ni(111) facet.
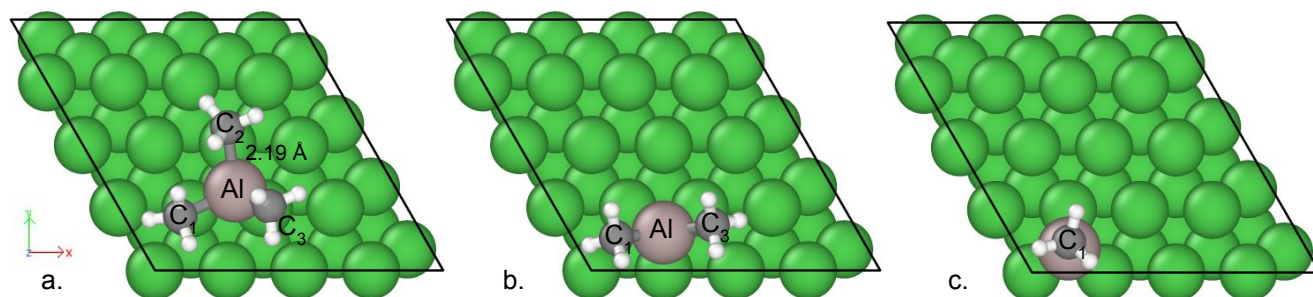
Figure 4: (a) TMA, (b) DMA, and (c) MA adsorption geometries on Ni(111)

Figure 5a and b details the top and side views of the Ni(211) facet with the step, terrace, and corner rows highlighted with dotted lines; the stepped nature of this facet creates a different chemical environment on each row with varying adsorption properties. In the case of the TMA, the orientation of the molecule influenced the adsorption strength. The strongest adsorption energy (-1.78 eV) was found when the TMA molecule is oriented as in Figures 5c and d, with the Al atom located on a three-fold adsorption site situated between the step and terrace rows and two of the CH_3 groups pointing towards the step row. This adsorption mode caused the scission of one of the Al-C bonds, leading to the formation of both the DMA intermediate and the CH_3 radical, with the CH_3 radical settling on a bridge position over the step row. Figure 5 also shows the converged geometries for the DMA (Figure 5e and f) and MA (Figure 5g and h) intermediates with adsorption energies of -3.12 and -3.33 eV, respectively. The increasing adsorption energies evidence a stronger interaction with the surface as the number of Al-C scissions increases. In all cases, the preferred adsorption in the vicinities of the step row evidences the increased reactivity due to the lower coordination of the nickel atoms that constitute the step row, compared to the coordination of nickel atoms on the terrace and corner rows. Table 1 summarizes the adsorption energies for the TMA molecule and its intermediates on the nickel oxide and metallic nickel facets studied.
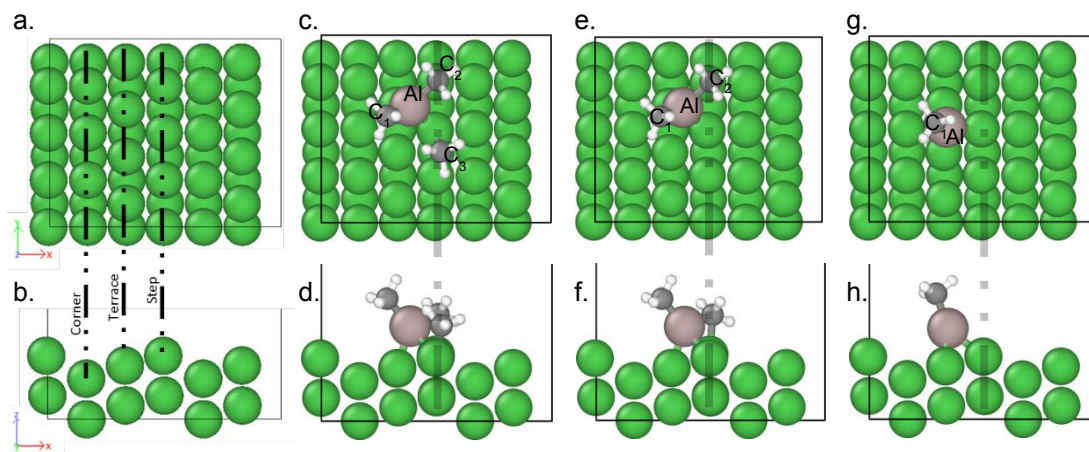
Figure 5: (a,b) Top and side views for Ni(211). TMA, DMA, and MA adsorption geometries on Ni(211): top and side views for (c,d) TMA, (e,f) DMA, and (g,h) MA

Table 1. Summary of the adsorption energy (eV) for each one of the principal molecular species (TMA, DMA, and MA) on the NiO and Ni surfaces.

System		Ads. E. (eV)		
		TMA	DMA	MA
NiO(100)		-1.24	-2.21	-1.45
NiO(111)	1-O site	-1.30	-2.82	-2.54
	2-O site	-0.29	-3.61	-2.66
Ni(111)		-0.95	-2.99	-3.75
Ni(211)		-1.78	-3.12	-3.33

CH$_3$ on NiO and Ni surface facets

Studying the CH$_3$ adsorption on NiO and Ni facets helped us to understand the likelihood of the CH$_3$ radicals to remain over the nanoparticle surface, limiting the number of adsorption sites available for the decomposition of further TMA molecules. In the case of the NiO(100) facet, the CH$_3$ radical does not adsorb on oxygen atoms but instead converges onto a nickel atom at 1.99 Å Ni-C distance and E_{ads} = -0.81 eV. Regardless of the favorable adsorption energy, the Bader charge analysis shows no significant electronic charge exchange between the CH$_3$ radical and the surface. On the NiO(111) facet with octopolar reconstruction, the CH$_3$ adsorption on oxygen was favorable only for the case of the CH$_3$ located on top of the outermost oxygen atom (oxygen site 1) at 1.44 Å with adsorption energy equal to -1.26 eV (Figures 6a and b). The Bader charge analysis for this adsorption mode revealed a net electronic charge transfer equal to 0.518 |e| from the CH$_3$ radical to the surface. The adsorption of the CH$_3$ radical on other sites over the NiO(111) facet converged to the CH$_3$ radical coordinating with either two or three nickel atoms. Figure 6c and d shows the case for the CH$_3$ coordinating with two nickel atoms at 2.16 and 2.24 Å, respectively, with E_{ads} = -1.11 eV, whereas Figures 6e and f shows the CH$_3$ coordinating with three nickel atoms at 2.39, 2.43, and 2.43 Å, with adsorption energy equal to -0.95 eV. The Bader charge analysis for these two cases revealed a net electronic charge transfer from the surface to the CH$_3$ radical equal to 0.439 and 0.468 |e|, respectively.

The adsorption for the CH$_3$ on a nickel site 2 was unfavorable (refer to blue colored sites in Figure 2 above). These series of calculations show that the adsorption of CH$_3$ on NiO(111) with octopolar reconstruction is highly dependent on the accessibility of the adsorption site.
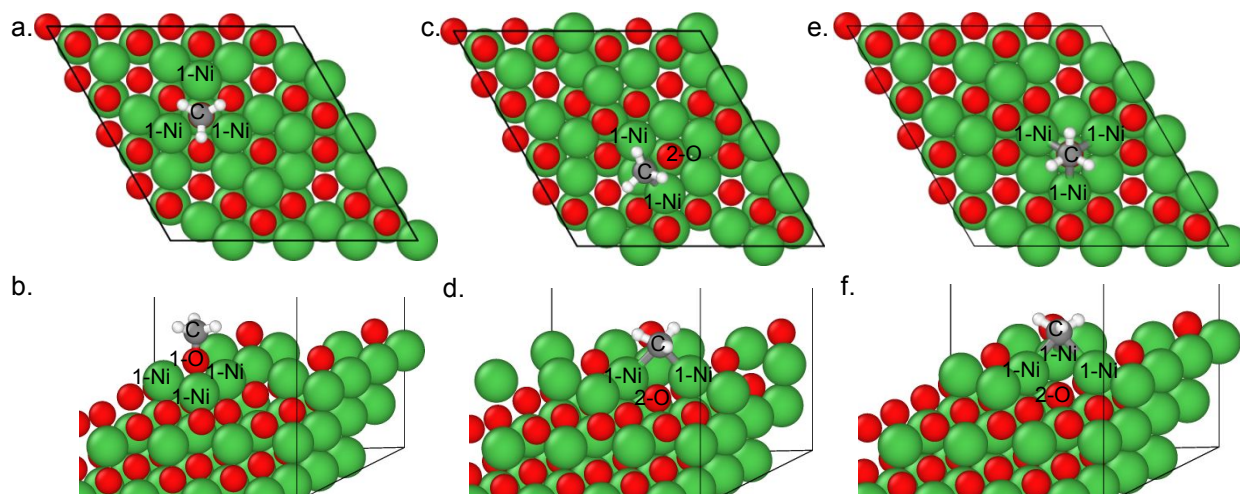
Figure 6: CH$_3$ radical on NiO(111): Top and side views for CH$_3$ on (a,b) oxygen site 1, (c,d) CH$_3$ on two nickel sites 1, (e,f) CH$_3$ on three nickel sites 1.

In the case of Ni(111), the CH$_3$ converged into a three-fold coordinated geometry (E$_{ads}$ = -1.95 eV), with no significant difference between the adsorption on either fcc or hcp sites. We also evaluated the adsorption of CH$_3$ on top of a nickel atom by limiting the movement of the CH$_3$ along the z-coordinate during the optimization, but the calculated adsorption energy is 0.30 eV less favorable compared to the adsorption on the three-fold fcc and hcp sites. For the Ni(211) facet, the CH$_3$ adsorption energy was stronger as the CH$_3$ converges into an adsorption site closer to the step row. The most favorable sites corresponded to the CH$_3$ on a three-coordinated site located between the step and terrace rows and the CH$_3$ on a bridge site over the step row, with adsorption energies equal to -2.14 and -2.05 eV, respectively. Figure 7 specifies the adsorption sites on the Ni(211) surface according to their distance to the step row. These series of calculations revealed stronger adsorption of CH$_3$ on metallic nickel than on nickel oxide. Among the metallic nickel facets, the calculations indicated stronger adsorption on the Ni(211) facet. Table 2 summarizes the adsorption energies for the CH$_3$ radical on the nickel oxide and metallic nickel facets studied. Calculations of the CH$_3$ adsorption on palladium surfaces reported adsorption energies of -1.88 eV and -2.03 eV on Pd(111) and Pd(211) facets,[14] comparable to our calculations on Ni surfaces. Even though we lack experimental data on the adsorption of CH$_3$ on nickel, experimental data with palladium nanoparticles shows that CH$_3$ is thermally stable up to 440 K.[46-47] The similarities between our calculations and the CH$_3$ adsorption on Pd(111) and Pd(211), together with the experimental data on the thermal stability of the CH$_3$ adsorption on palladium nanoparticles, leads us to believe that CH$_3$ species are likely to remain on the surface and act as contaminants in the Al$_2$O$_3$ ALD deposition on nickel nanoparticles.
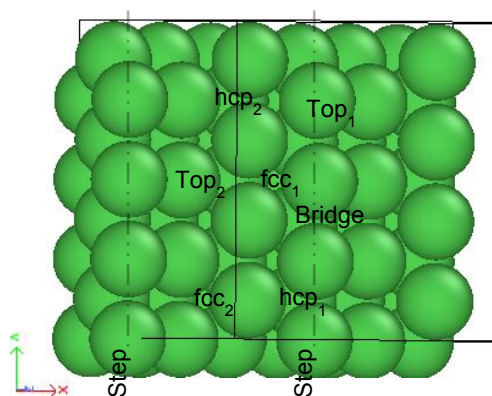
Figure 7. Favorable adsorption sites evaluated on Ni(211) surface. Vertical dashed lines show the location of the steps.

8

Table 2. Summary of CH$_3$ adsorption energies on NiO and Ni surfaces.

NiO(100)		NiO(111)		Ni(111)		Ni(211)	
Ads. Site	Ads. En. [eV]	Ads. Site	Ads. En. [eV]	Ads. Site	Ads. En. [eV]	Ads. Site	Ads. En. [eV]
Ni-Ni Bridge	-0.74	1-O	-1.26	fcc	-1.95	Bridge	-2.14
Ni-O Bridge	-0.74	2-O	-0.95	hcp	-1.92	Top$_1$	-1.85
Ni Top	-0.81	3-O	-1.07	Bridge	-1.94	fcc$_1$	-1.90
O Top	0.01	4-O	-1.07	Top	-1.64	hcp$_1$	-2.05
--	--	1-Ni	-1.11	--	--	fcc$_2$	-1.28
--	--	2-Ni	0.40	--	--	Top$_2$	-1.49
--	--	--	--	--	--	hcp$_2$	-1.58

TMA decomposition mechanism

The next step in our work was the calculation of the reaction energies and reaction barriers following the decomposition mechanism of the TMA molecule outlined in equations (1) to (3).[14] In this mechanism, the dissociative adsorption of the TMA molecule passes through the sequential scission of Al-C bonds, leading to the successive formation of the DMA and MA intermediates, finishing with adsorbed Al atoms. Theoretically, the CH$_3$ radicals react with preadsorbed H to desorb in the form of CH$_4$. However, earlier studies have detected C$_2$H$_6$ as reaction product besides the CH$_4$ (mainly during the first ALD cycle) attributed to possible coupling reactions between adjacent CH$_3$ species.[14] Here we did not address the desorption mechanisms of the CH$_3$ radicals but rather focused on the scission of the Al-C bonds and the adsorption of the formed CH$_3$ radical.

Al(CH$_3$)$_3^*$ + * → Al(CH$_3$)$_2^*$ + CH$_3^*$ eq. 1

Al(CH$_3$)$_2^*$ + * → Al(CH$_3$)* + CH$_3^*$ eq. 2

Al(CH$_3$)* + * → Al* + CH$_3^*$ eq. 3
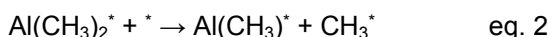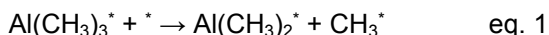
Figure 8 summarizes the reaction energy profiles for the decomposition of the TMA molecule on each of the oxidized and metallic nickel facets studied here. The horizontal axes correspond to the reaction coordinate, the images 0 and 4 correspond to the initial and final states, respectively, and the intermediates are images 1, 2, and 3. Depending on the specifics of each reaction, the location of the transition state (TS) corresponds to the maximum in the energy profile. The TS geometries are shown in Figure 8 (the overall reaction from reactant, intermediate species, to product is illustrated in Figures S1 to S3 in the supporting information). The dotted patterns in blue and green correspond to the NiO(100) and NiO(111) facets, respectively, whereas the continuous red and black profiles correspond to the Ni(111) and Ni(211) facets. For the NiO(100) facet, the decomposition of the TMA molecule towards the DMA intermediate and the CH$_3$ radical (Figure8a) is an endothermic process and has an energy barrier as high as 2.97 eV, but this pattern changes for the NiO(111) facet, displaying an exothermic behavior with an energy barrier 2.28 eV lower compared to the NiO(100). In the case of the metallic facets, the TMA decomposition on Ni(111) is a barrierless process with a reaction energy equal to -0.31 eV. The Ni(211) showed higher reactivity for the TMA decomposition compared to the Ni(111), as the mere adsorption of the TMA molecule caused the scission of one Al-C leading the spontaneous formation of the DMA intermediate and the CH$_3$ radical.

Energy profiles   **Transition states**
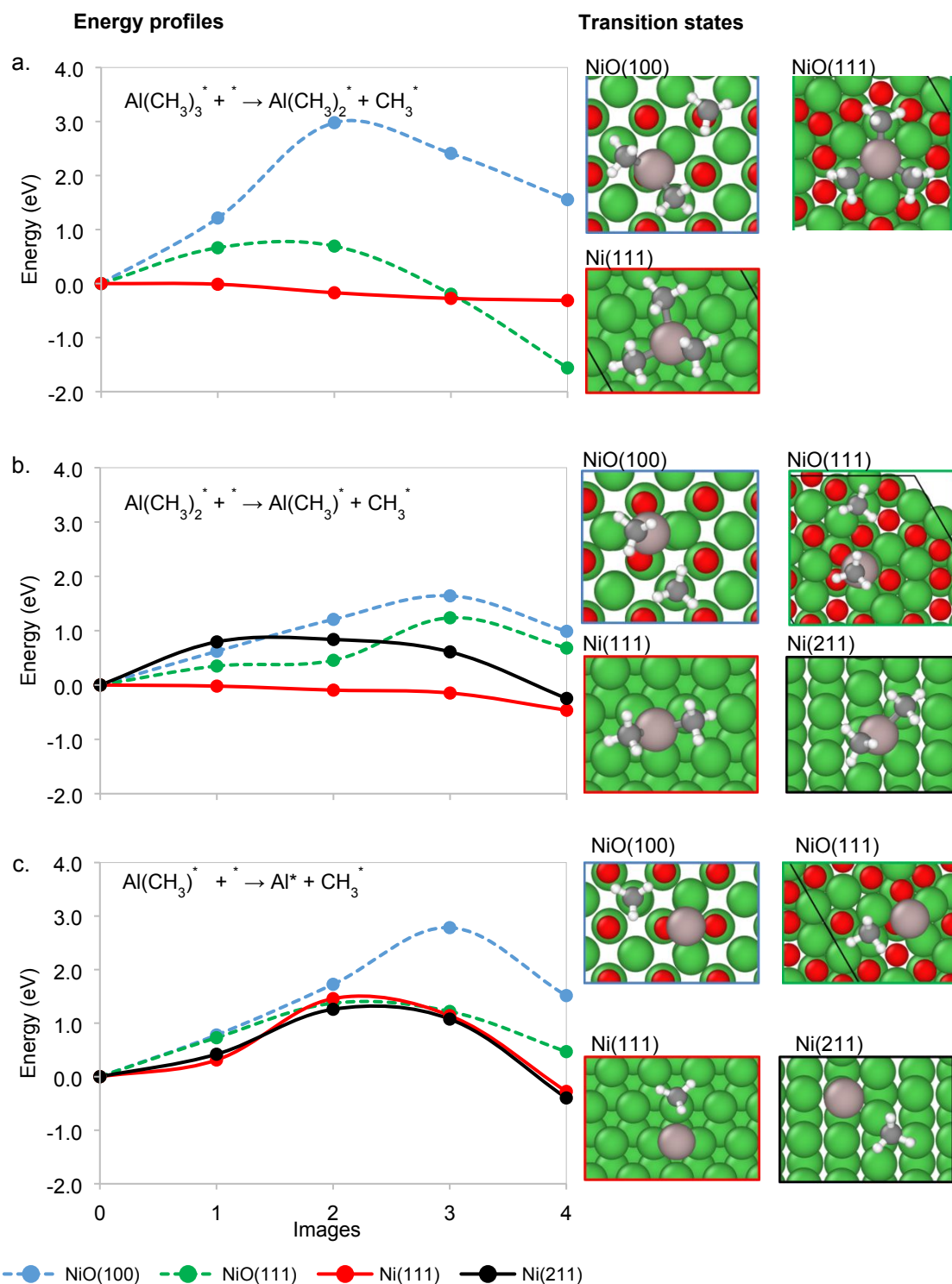
Figure 8: Left: reaction energy profiles for the decomposition of (a) TMA molecule; (b) DMA; and (c) MA intermediates on NiO(100) (blue), NiO(111) (green), Ni(111) (red), and Ni(211) (black). Right: Transition states for each reaction. Neither the energy profile nor the transition state for the decomposition of the TMA molecule on Ni(211) are shown as this is a barrierless process.

Regarding the decomposition of the DMA intermediate into MA and CH_3 (Figure 8b), both nickel oxide facets display positive reaction energies equal to 0.99 and 0.68 eV and energy barriers equal to 1.64 and 1.24 eV on NiO(100) and NiO(111), respectively. In a similar manner to the behavior displayed for the TMA molecule, the

NiO(111) shows better favorability for the decomposition of the DMA intermediate compared to the NiO(100). Both Ni(111) and Ni(211) show a slightly exothermic behavior for the DMA decomposition with reaction energies equal to -0.47 and -0.25 eV, respectively. Interestingly, the reaction barriers for these two facets suggest higher reactivity for the Ni(111) compared to the Ni(211) facet as the energy profile on Ni(111) is barrierless whereas the one for the Ni(211) has an energy barrier of 0.84 eV.

The energy profiles in Figure 8c correspond to the MA decomposition into Al and CH_3. The reaction energy on NiO(100) is 1.52 eV, while the energy barrier is as high as 2.78 eV. This endothermic pattern coupled with the high reaction barrier hint to a unfavorable decomposition of MA on NiO(100). The NiO(111) facet displays a behavior similar to the NiO(100), but the reaction energy is 1.04 eV less endothermic and the energy barrier is only 1.37 eV, significantly lower compared to the energy barrier on NiO(100). Once again, the carved out topology of the NiO(111) facet shows higher reactivity towards the MA decomposition, compared to the flat NiO(100) facet. On Ni(111) and Ni(211), both facets display exothermic profiles for the MA decomposition with reaction energies equal to -0.28 and -0.40 eV, respectively. The energy barriers on these metallic facets are comparable to the reaction barrier for the MA decomposition on NiO(111), with 1.46   and 1.26 eV on Ni(111) and Ni(211), respectively.

Compared to nickel oxide, the metallic facets showed similar to lower energy barriers and tend to be more thermodynamically favorable throughout the three decomposition reactions. On Ni(111), the decomposition mechanism followed through the scission of the elongated Al-CH_3 bond in the adsorption mode of the TMA molecule (see Figure 4 above). Figure 9a shows the geometry for the DMA intermediate and the CH_3 radical on Ni(111). The cleavage of the Al-CH_3 bond led to the displacement of the Al atom towards an adjacent adsorption site and the CH_3 deposition on a neighboring three-fold adsorption site at 4.55 Å from the DMA intermediate.

The Ni(211) facet, on the other side, showed higher reactivity compared to Ni(111) as the adsorption mode of the TMA molecule caused the scission of the Al-CH_3 bond (geometry in Figure 9 on the right hand side). The underlying cause for the higher reactivity of the Ni(211) facet is the lower coordination of the Ni atoms along the step row compared to the other rows away for the edge.
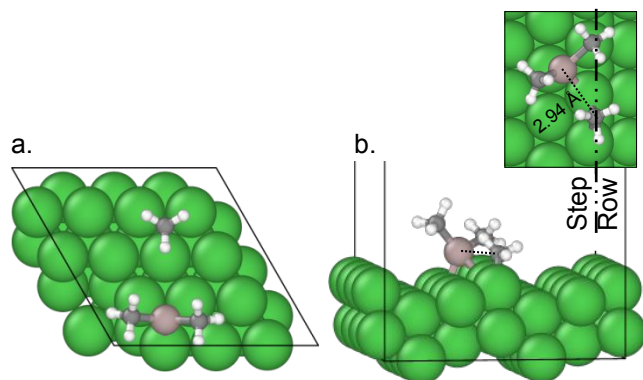
Figure 9: (a) DMA and CH_3 adsorption geometries on Ni(111), (b) TMA on Ni(211) with the inset showing the top view.

The decomposition of the DMA intermediate into MA and CH_3 reveals the impact of the step row on the dissociation mechanism. Figure 10a and b shows that on Ni(111) the decomposition products of the DMA intermediate both settle on three-fold coordinated adsorption sites separated 3.97 Å. On Ni(211), however, only the MA intermediate settles on a three-fold coordinate adsorption site, whereas the CH_3 adsorbs on a bridge position along the step row separated 4.33 Å from the MA (Figures 10c and d).
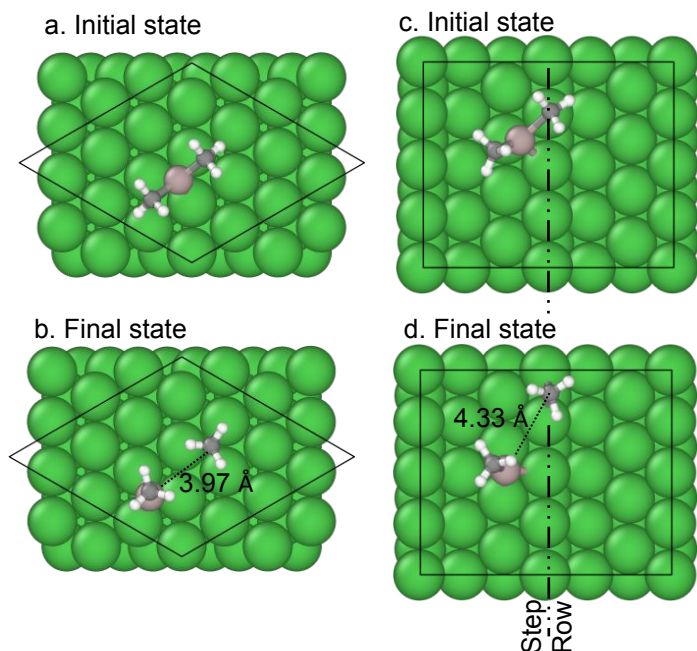
Figure 10: Initial and final states for the DMA dissociation on (a,b) Ni(111) and (c,d) Ni(211)

Figure 11 points out again the impact of the step row on the Ni(211) facet on the dynamics of the decomposition of the MA intermediate into Al and CH_3. Regardless of the similarities of the energy profiles on both metallic facets (Figure 8c), Figure 10 shows that on Ni(111) the mobility of the decomposition products is lower compared to Ni(211). We have inferred the mobility behavior based on how much the atoms tend to move on the surface to find a more stable location during the geometry optimization. On Ni(111), the Al formed upon the Al-C scission migrates between adjacent three-fold adsorption sites and the CH_3 adsorbs on another three-fold adsorption site 4.41 Å distant from the Al atom. On the other side, the Al atom on Ni(211) shows a larger displacement from the step row towards the corner row whereas the CH_3 settles on a bridge site along the step row 5.11 Å away from the Al atom. As we can consider the Ni(211) facet as tilted Ni(111) planes stacked one above another, we attribute the higher mobility of the decomposition products on Ni(211) to changes in the chemical environment of the surface near to the edge of the Ni(111) facet.

Our calculations on metallic nickel facets show that presence of edges and defects with low coordination effectively impacts the decomposition mechanisms compared to flat facets but this effect is less significant compared to those on other metals such as palladium and platinum where the differences in the reaction energies and energy barriers have shown to be more significant.[14, 16] This behavior with metallic nickel facets suggests a less likelihood for the occurrence of an island coalescence mechanism that initiates the Al_2O_3 growth on discrete sites over the nanoparticle surface, but a higher likelihood of a uniform dispersion of the Al_2O_3 seeds over the surface at the early stages of growth.

Both nickel oxide facets consistently show less exothermic behavior and higher reaction barriers compared to the metallic facets. Even though the experimental evidence shows that Al_2O_3 ALD is effectively possible on nickel oxide nanoparticles,[4] our calculations suggest a less favorable decomposition of the TMA molecule that might impact the growth dynamics during the first round of TMA exposure of the nickel oxide nanoparticle. Moreover, the flat NiO(100) facet consistently shows higher reaction barriers compared to the NiO(111) facet with carved out topology. Moreover, the surface reconstruction observed in NiO(111) after MA adsorption, suggests the possible impact that the strong reducing nature of TMA might induce triggering preferred decomposition on corner or edges motifs present on nickel oxide particles. This behavior points to a possible island coalescence mechanism governing the early stages of the Al_2O_3 growth on nickel oxide.
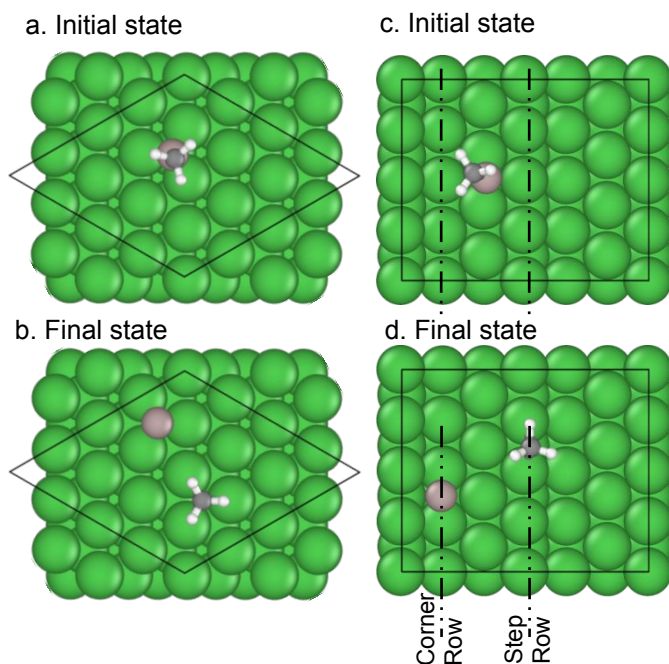
Figure 11: Initial and final states for the MA dissociation on (a,b) Ni(111) and (c,d) Ni(211). Dashed vertical lines illustrate positions of corner and step rows.

Another interesting feature is the energy of adsorption of the CH_3 radical formed in the decomposition reactions. Figure 12 compares the adsorption energy of the CH_3 radicals on nickel oxide and metallic nickel facets. The metallic facets show better affinity towards the adsorption of CH_3 compared to nickel oxide surfaces, and the Ni(211) shows the strongest adsorption energy among all facets. We observe a correlation between the higher reactivity of metallic nickel facets and the more favorable adsorption of CH_3 radicals, and we believe that this behavior might have an impact of the morphology of the Al_2O_3 coating formed upon ALD treatment. The strong adsorption of CH_3 on metallic nickel might make difficult the desorption of the CH_3 radicals therefore limiting further decomposition of TMA molecules due to contamination. However, it is possible that this contamination can trigger the growth of a porous coating, and the voids created upon removal of CH_3 (with thermal treatment) can contribute to generating diffusion paths allowing easier access to the catalytic surfaces.
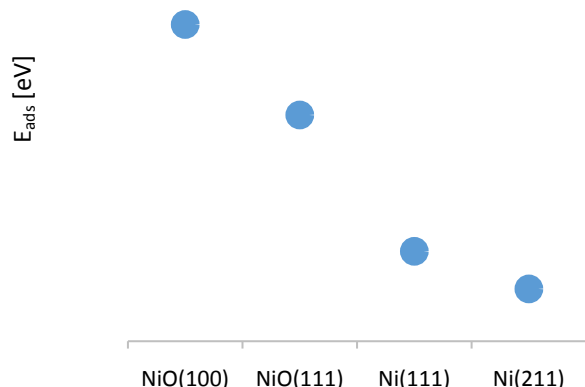
Figure 12: Adsorption energy of CH_3 on oxidized and metallic nickel facets.

Conclusions

Our DFT calculations show that TMA decomposition is more favorable on metallic nickel than on nickel oxide facets. Beside, we observe similar reaction energy profiles on flat Ni(111) and stepped Ni(211). This behavior shows the reactivity of both facets towards TMA decomposition and makes less likely the possibility of an island coalescence growth mechanism on metallic nickel nanoparticles, as has been suggested for the Al_2O_3 ALD growth on Pd and Pt. On the other hand, both NiO(100) and NiO(111) show endothermic reaction energies and high energy barriers for the decomposition of TMA that suggest a rather low favorability on the very earlier stages of the Al_2O_3 grown on oxidized nickel nanoparticles. Between these two nickel oxide facets, however, the more favorable reaction energies and lower reaction barriers observed on the NiO(111) surface, suggest more favorable TMA decomposition on carved out topologies than on flat facets due to the higher reactivity of the oxygen atoms located on the most external layers formed after the octopolar reconstruction. Regarding to the adsorption of the CH_3 radicals formed upon scission of the Al-C atoms, the metallic facets are more favorable towards the CH_3 adsorption compared to nickel oxide. The Ni(211) shows the strongest adsorption among all facets, and these adsorption energies are comparable to the adsorption energies calculated in earlier works on Al_2O_3 ALD growth on palladium surfaces, where the experiments show the CH_3 adsorption to be thermally stable up to 440K. We observe a correlation between the higher reactivity of metallic nickel facets and the more favorable adsorption of CH_3 radicals, and we believe this behavior might promote the growth of a porous Al_2O_3 coating due to CH_3 contamination rather than to preferential TMA decomposition, as earlier works on Pd and Pt suggest.

Conflicts of Interest

There are no conflicts of interest to declare

Acknowledgements

References

1. Usman, M.; Wan Daud, W. M. A.; Abbas, H. F., Dry reforming of methane: Influence of process parameters—A review. *Renewable Sustainable Energy Rev.* **2015,** *45*, 710-744.
2. Wang, S.; Lu, G. Q.; Millar, G. J., Carbon Dioxide Reforming of Methane To Produce Synthesis Gas over Metal-Supported Catalysts: State of the Art. *Energy & Fuels* **1996,** *10* (4), 896-904.
3. Guo, J.; Lou, H.; Zhao, H.; Chai, D.; Zheng, X., Dry reforming of methane over nickel catalysts supported on magnesium aluminate spinels. *Applied Catalysis A: General* **2004,** *273* (1), 75-82.
4. Baktash, E.; Littlewood, P.; Schomäcker, R.; Thomas, A.; Stair, P. C., Alumina coated nickel nanoparticles as a highly active catalyst for dry reforming of methane. *Appl. Catal., B* **2015,** *179*, 122-127.
5. Pakhare, D.; Spivey, J., A review of dry (CO2) reforming of methane over noble metal catalysts. *Chem. Soc. Rev.* **2014,** *43* (22), 7813-7837.
6. Gould, T. D.; Izar, A.; Weimer, A. W.; Falconer, J. L.; Medlin, J. W., Stabilizing Ni Catalysts by Molecular Layer Deposition for Harsh, Dry Reforming Conditions. *ACS Catal.* **2014,** *4* (8), 2714-2717.
7. Ding, L.; Yi, H.; Zhang, W.; You, R.; Cao, T.; Yang, J.; Lu, J.; Huang, W., Activating Edge Sites on Pd Catalysts for Selective Hydrogenation of Acetylene via Selective Ga2O3 Decoration. *ACS Catalysis* **2016,** *6* (6), 3700-3707.
8. Lu, J.; Fu, B.; Kung, M. C.; Xiao, G.; Elam, J. W.; Kung, H. H.; Stair, P. C., Coking- and Sintering-Resistant Palladium Catalysts Achieved Through Atomic Layer Deposition. *Science* **2012,** *335* (6073), 1205.

9. Yi, H.; Du, H.; Hu, Y.; Yan, H.; Jiang, H.-L.; Lu, J., Precisely Controlled Porous Alumina Overcoating on Pd Catalyst by Atomic Layer Deposition: Enhanced Selectivity and Durability in Hydrogenation of 1,3-Butadiene. *ACS Catal.* **2015,** *5* (5), 2735-2739.

10. Lu, J.; Elam, J. W.; Stair, P. C., Atomic layer deposition—Sequential self-limiting surface reactions for advanced catalyst "bottom-up" synthesis. *Surface Science Reports* **2016,** *71* (2), 410-472.

11. Puurunen, R. L., Surface chemistry of atomic layer deposition: A case study for the trimethylaluminum/water process. *J. Appl. Phys.* **2005,** *97* (12), 9.

12. Ritala, M.; Leskelä, M.; Dekker, J. P.; Mutsaers, C.; Soininen, P. J.; Skarp, J., Perfectly conformal TiN and Al2O3 films deposited by atomic layer deposition. *Chem. Vap. Deposition* **1999,** *5* (1), 7-9.

13. Leskelä, M.; Ritala, M., Atomic layer deposition (ALD): from precursors to thin film structures. *Thin Solid Films* **2002,** *409* (1), 138-146.

14. Lu, J.; Liu, B.; Greeley, J. P.; Feng, Z.; Libera, J. A.; Lei, Y.; Bedzyk, M. J.; Stair, P. C.; Elam, J. W., Porous Alumina Protective Coatings on Palladium Nanoparticles by Self-Poisoned Atomic Layer Deposition. *Chem. Mater.* **2012,** *24* (11), 2047-2055.

15. Rahtu, A.; Alaranta, T.; Ritala, M., In Situ Quartz Crystal Microbalance and Quadrupole Mass Spectrometry Studies of Atomic Layer Deposition of Aluminum Oxide from Trimethylaluminum and Water. *Langmuir* **2001,** *17* (21), 6506-6509.

16. Lu, J.; Liu, B.; Guisinger, N. P.; Stair, P. C.; Greeley, J. P.; Elam, J. W., First-Principles Predictions and in Situ Experimental Validation of Alumina Atomic Layer Deposition on Metal Surfaces. *Chem. Mater.* **2014,** *26* (23), 6752-6761.

17. Lu, J.; Low, K.-B.; Lei, Y.; Libera, J. A.; Nicholls, A.; Stair, P. C.; Elam, J. W., Toward atomically-precise synthesis of supported bimetallic nanoparticles using atomic layer deposition. *Nat. Commun.* **2014,** *5*, 3264.

18. O'Neill, B. J.; Jackson, D. H. K.; Crisci, A. J.; Farberow, C. A.; Shi, F.; Alba-Rubio, A. C.; Lu, J.; Dietrich, P. J.; Gu, X.; Marshall, C. L.; Stair, P. C.; Elam, J. W.; Miller, J. T.; Ribeiro, F. H.; Voyles, P. M.; Greeley, J.; Mavrikakis, M.; Scott, S. L.; Kuech, T. F.; Dumesic, J. A., Stabilization of Copper Catalysts for Liquid-Phase Reactions by Atomic Layer Deposition. *Angewandte Chemie International Edition* **2013,** *52* (51), 13808-13812.

19. Blöchl, P. E., Projector augmented-wave method. *Phys. Rev. B* **1994,** *50* (24), 17953.

20. Perdew, J. P.; Burke, K.; Ernzerhof, M., Generalized gradient approximation made simple. *Phys. Rev. Lett.* **1996,** *77* (18), 3865.

21. Perdew, J. P.; Burke, K.; Ernzerhof, M., Generalized Gradient Approximation Made Simple [Phys. Rev. Lett. 77, 3865 (1996)]. *Phys. Rev. Lett.* **1997,** *78* (7), 1396-1396.

22. Monkhorst, H. J.; Pack, J. D., Special points for Brillouin-zone integrations. *Phys. Rev. B* **1976,** *13* (12), 5188.

23. Ebensperger, C.; Meyer, B., First-principles study of the reconstruction and hydroxylation of the polar NiO (111) surface. *physica status solidi (b)* **2011,** *248* (10), 2229-2241.

24. Zhu, Y.-A.; Chen, D.; Zhou, X.-G.; Yuan, W.-K., DFT studies of dry reforming of methane on Ni catalyst. *Catal. Today* **2009,** *148* (3), 260-267.

25. Methfessel, M.; Paxton, A., High-precision sampling for Brillouin-zone integration in metals. *Phys. Rev. B* **1989,** *40* (6), 3616.

26. Blöchl, P. E.; Jepsen, O.; Andersen, O. K., Improved tetrahedron method for Brillouin-zone integrations. *Phys. Rev. B* **1994,** *49* (23), 16223-16233.

27. Rohrbach, A.; Hafner, J.; Kresse, G., Molecular adsorption on the surface of strongly correlated transition-metal oxides: A case study for CO/NiO(100). *Phys. Rev. B* **2004,** *69* (7), 075413.

28. Anisimov, V. I.; Zaanen, J.; Andersen, O. K., Band theory and Mott insulators: Hubbard U instead of Stoner I. *Phys. Rev. B* **1991,** *44* (3), 943.

29. Bengone, O.; Alouani, M.; Blöchl, P.; Hugel, J., Implementation of the projector augmented-wave LDA+U method: Application to the electronic structure of NiO. *Phys. Rev. B* **2000,** *62* (24), 16392.

30. Bengone, O.; Alouani, M.; Hugel, J.; Blöchl, P., LDA+U calculated electronic and structural properties of NiO(001) and NiO(111) p(2×2) surfaces. *Comput. Mater. Sci.* **2002,** *24* (1), 192-198.

31. Zhang, W.-B.; Tang, B.-Y., Stability of the polar NiO(111) surface. *J. Chem. Phys.* **2008,** *128* (12), 124703.

32. Wang, S.-G.; Cao, D.-B.; Li, Y.-W.; Wang, J.; Jiao, H., CO2 Reforming of CH4 on Ni(111): A Density Functional Theory Calculation. *J. Phys. Chem. B* **2006,** *110* (20), 9976-9983.

33. Henkelman, G.; Uberuaga, B. P.; Jónsson, H., A climbing image nudged elastic band method for finding saddle points and minimum energy paths. *J. Chem. Phys.* **2000,** *113* (22), 9901-9904.

34. Henkelman, G.; Jónsson, H., Improved tangent estimate in the nudged elastic band method for finding minimum energy paths and saddle points. *J. Chem. Phys.* **2000,** *113* (22), 9978-9985.

35. Tang, W.; Sanville, E.; Henkelman, G., A grid-based Bader analysis algorithm without lattice bias. *J. Phys.: Condens. Matter* **2009,** *21* (8), 084204.

36.   Sanville, E.; Kenny, S. D.; Smith, R.; Henkelman, G., Improved grid-based algorithm for Bader charge allocation. *J. Comput. Chem.* **2007,** *28* (5), 899-908.

37.   Henkelman, G.; Arnaldsson, A.; Jónsson, H., A fast and robust algorithm for Bader decomposition of charge density. *Comput. Mater. Sci.* **2006,** *36* (3), 354-360.

38.   Cappus, D.; Xu, C.; Ehrlich, D.; Dillmann, B.; Ventrice, C. A.; Al Shamery, K.; Kuhlenbeck, H.; Freund, H. J., Hydroxyl groups on oxide surfaces: NiO(100), NiO(111) and Cr2O3(111). *Chemical Physics* **1993,** *177* (2), 533-546.

39.   Fisher, C. A. J., Molecular dynamics simulations of reconstructed NiO surfaces. *Scr. Mater.* **2004,** *50* (7), 1045-1049.

40.   Wolf, D., Reconstruction of NaCl surfaces from a dipolar solution to the Madelung problem. *Phys. Rev. Lett.* **1992,** *68* (22), 3315.

41.   Kuhlenbeck, H.; Shaikhutdinov, S.; Freund, H.-J., Well-ordered transition metal oxide layers in model catalysis–a series of case studies. *Chem. Rev.* **2013,** *113* (6), 3986-4034.

42.   Barbier, A.; Renaud, G., Structural investigation of the NiO (111) single crystal surface. *Surface Science* **1997,** *392* (1-3), L15-L20.

43.   Juppo, M.; Alén, P.; Ritala, M.; Leskelä, M., Trimethylaluminum as a Reducing Agent in the Atomic Layer Deposition of Ti(Al)N Thin Films. *Chemical Vapor Deposition* **2001,** *7* (5), 211-217.

44.   Alén, P.; Juppo, M.; Ritala, M.; Sajavaara, T.; Keinonen, J.; Leskelä, M., Atomic Layer Deposition of Ta(Al)N(C) Thin Films Using Trimethylaluminum as a Reducing Agent. *J. Electrochem. Soc.* **2001,** *148* (10), G566-G571.

45.   Schmidt, D.; Knaut, M.; Hossbach, C.; Albert, M.; Dussarrat, C.; Hintze, B.; Bartha, J. W., Atomic Layer Deposition of Ta–N-Based Thin Films Using a Tantalum Source. *J. Electrochem. Soc.* **2010,** *157* (6), H638-H642.

46.   Levis, R. J.; Zhicheng, J.; Winograd, N., Thermal decomposition of methanol absorbed on palladium{111}. A new reaction pathway involving methyl formation. *J. Am. Chem. Soc.* **1989,** *111* (13), 4605-4612.

47.   Kruse, N.; Rebholz, M.; Matolin, V.; Chuah, G. K.; Block, J. H., Methanol decomposition on Pd(111) single crystal surfaces. *Surface Science* **1990,** *238* (1), L457-L462.